Electronic energy scales of CrX_3 (X = Cl, Br, and I) using high-resolution x-ray scattering

Chamini S. Pathiraja,[1] Jayajeewana N. Ranhili,[1] Deniz Wong,[2] Christian Schulz,[2] Yi-De Chuang,[3] Yu-Cheng Shao,[4] Di-Jing Huang,[4] Hsiao-Yu Huang,[4] Amol Singh,[4] and Byron Freelon[1,*]

[1]*Physics Department and Texas Center for Superconductivity, University of Houston, Houston, Texas 77204, USA*

[2]*Helmholtz-Zentrum Berlin für Materialien und Energie, D-14109 Berlin, Germany*

[3]*Lawrence Berkeley National Laboratory, Berkeley, California 94720, USA*

[4]*National Synchrotron Radiation Research Center, 101 Hsin-Ann Road, Hsinchu Science Park, Hsinchu 30076, Taiwan*

(Received 2 December 2024; accepted 23 September 2025; published 6 November 2025)

Chromium trihalides CrX_3 (X = Cl, Br, and I) have recently become a focal point of research due to their intriguing low-temperature, layer-dependent magnetic properties that can be manipulated by external stimuli. This makes them essential candidates for spintronic applications. Their magnetic orders are often related to the electronic structure parameters, such as spin-orbit coupling (SOC), Hund's coupling (J_H), p–d covalency, and interorbital Coulomb interactions. Accurately determining such parameters is paramount for understanding CrX_3 physics. We have used high-resolution resonant inelastic x-ray scattering spectroscopy to study CrX_3 across phase transition temperatures. Ligand field multiplet calculations were used to determine the electronic structure parameters by incorporating the crystal field interactions in a distorted octahedral orientation with C_3 symmetry. These methods provide the most detailed description of CrX_3 magneto-optical and electronic (energetic) terms to date. The crystal field distortion parameters $D\sigma$ and $D\tau$ were experimentally determined, and the energies of d orbitals have been reported. The spectroscopic measurements reveal an energy separation between spin-allowed quartet states and spin-forbidden doublet states, which increases upon going from $CrCl_3$ to CrI_3. The role of SOC, for Cr $2p$ orbitals, in spin-flip excitations has been demonstrated. The determined $10Dq$ values are in good agreement with the spectrochemical series, and Racah B follows the nephelauxetic effect. Such precise measurements offer insights into the energy design of spintronic devices that utilize quantum state tuning within two-dimensional magnetic materials.

DOI: 10.1103/jdxn-5lw4

I. INTRODUCTION

The chromium trihalides CrX_3 (X = Cl, Br, and I) compounds have ferromagnetic (FM) order in the monolayer limit with Curie temperatures T_c = 17, 34, and 61 K for bulk $CrCl_3$, $CrBr_3$, and CrI_3, respectively [1–3]. The interlayer interactions in bulk $CrCl_3$ are antiferromagnetic, while $CrBr_3$ and CrI_3 exhibit FM order. Electronegativity between metal Cr and the halides decreases as the halogen changes from Cl to Br to I [4–6]. This results in an increase in p–d covalency from $CrCl_3$ to CrI_3. With the presence of spin-orbit coupling (SOC), the FM superexchange interaction across the ∼90° Cr–X–Cr bonds becomes highly anisotropic in the edge-shared octahedral orientation in CrX_6 [see Fig. 1(a)] [7]. The produced magnetocrystalline anisotropy stabilizes the magnetic order in CrX_3, overcoming the Mermin-Wagner theorem [8,9] and leads to rich phase diagrams in CrX_3. This magnetic ordering appears to be dependent on the dimensionality, the atomic halogen constituents, layer interactions, and temperature. The electronic structure in the two-dimensional (2D) magnetic materials reveals a strong interplay between the material's atomic structure, spin interaction, and the movement of electrons, which are crucial for applications in spintronics and data storage [5,10]. Understanding magnetism also appears to be linked to determining the electronic levels of chromium bands near the Fermi energy. These circumstances suggest that obtaining precisely determined energy scales is an important for constructing theoretical models that explain the magnetic ground states (GSs) of CrX_3. The development of a high-accuracy Hamiltonian for CrX_3, supported by experimental findings, is urgently needed to enhance the ability of the condensed matter physics community to utilize these intriguing materials. These findings could impact the field of spin-based electronics since magnetism in CrX_3 compounds may be exploitable in the next generation of smart electronic devices, potentially surpassing the capabilities of graphene [11–17].

Measurements, including infrared spectroscopy, optical absorption spectroscopy, Raman spectroscopy, and x-ray photoemission spectroscopy, have been identified as excellent techniques for probing electronic transitions and determining the electronic structure of transition metal (TM) halides [18–21]. However, a significant challenge arises from the excitations between d orbitals being dipole forbidden [22,23]. Even though some dd transitions can be observed with low intensity, electronic transitions with different spin multiplicities remain optically undetectable. This underscores the necessity

*Contact author: bkfreelo@central.uh.edu

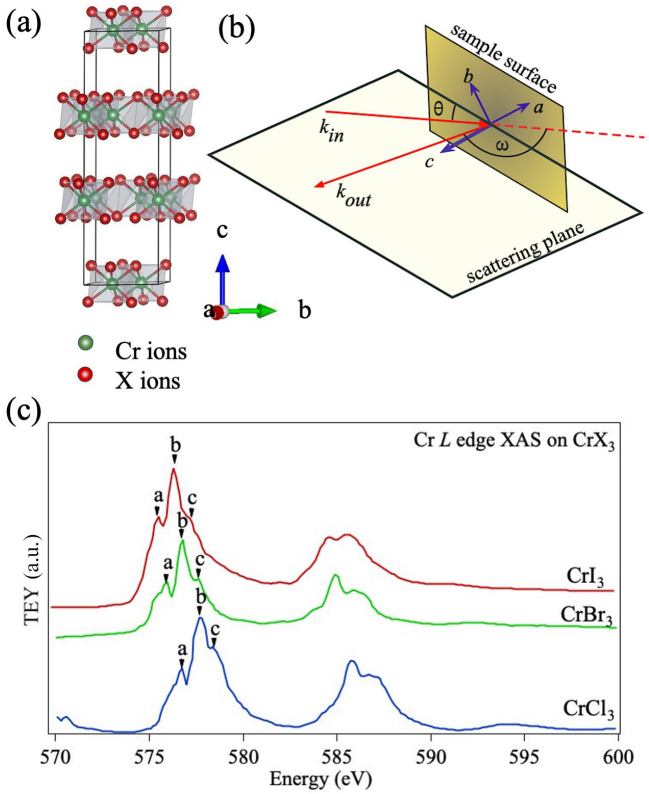

FIG. 1. (a) Lattice structure of CrX_3. The metal Cr and halide ions (X = Cl, Br, and I) are shown in green and red, respectively. (b) The schematic diagram illustrates the experimental setup for resonant inelastic x-ray scattering (RIXS) measurements. $\boldsymbol{k}_{\mathbf{in}}$ and $\boldsymbol{k}_{\boldsymbol{out}}$ are the incident and scattered photon beam wave vectors. (c) Cr L-edge x-ray absorption spectroscopy (XAS) measurements on CrX_3 (X = Cl, Br, and I). The photon energies labeled **a**, **b**, and **c** were used as the excitation energies in the RIXS measurements.

for spectroscopic probes that detect all potential dd transitions in order to determine a more accurate electronic structure in TM halides. With the development of 3rd generation synchrotrons, XAS, along with RIXS, has been used to probe the dd and charge-transfer (CT) excitations in TM complexes [4,9,24–27]. Cr L_3-edge RIXS is a resonant two-photon process ($2p \rightarrow 3d$ followed by $3d \rightarrow 2p$) that offers more flexibility in terms of selection rules compared to optical spectroscopy, primarily due to the core-hole intermediate state (IS) and its associated dynamics and interactions. The strong $2p$ core hole SOC permits the spin-selection rule to be alleviated, allowing for the probing of transitions that are spin-forbidden in optical spectroscopy. RIXS has been demonstrated to be a suitable tool for providing detailed electronic structure information in CrX_3, with the state- and element-selective measurement capability providing detailed investigations in atomic, crystal field, and charge-transfer information [4,9,28].

This paper reports enhanced RIXS spectral features in CrX_3 using high-resolution spectroscopic measurements. A significant outcome of our study is the first experimental observation of a considerable energy separation between the spin-allowed quartet and spin-forbidden doublet states in CrX_3. This energy gap shows an increment as the halogen changes from Cl to I. The Tanabe-Sugano-like energy level diagrams (ELDs) have been calculated and compared with the experimental RIXS spectra to determine the energy scales, such as crystal field splitting and Racah parameters. Atomic multiplet $2p$–$3d$ RIXS calculations have been performed to reconstruct the experimental RIXS spectra, and the electronic structure parameters across all halide systems in CrX_3 have been summarized.

II. METHOD

A. Experimental method

We performed Cr L-edge high-resolution RIXS measurements on CrX_3 at the 41A RIXS beamline of the Taiwan Photon Source [24]. Figure 1(b) illustrates the scattering geometry of RIXS measurements. The crystalline c axis was aligned within the horizontal scattering plane (π-polarization) during the measurements. The ab plane was unaligned, and the momentum dependence was not considered in this experiment. Cr L-edge XAS data were acquired prior to the RIXS measurements to determine the excitation photon energies. For the RIXS measurements, the tuned incident soft x-rays were directed at an angle (θ) of 90° to the sample surface (normal incidence), and the spectrometer was set at 140° (ω) backscattering geometry with respect to the incoming photon beam. The instrumental energy resolution was ~30 meV.

Complementary XAS and RIXS measurements were performed at the PEAXIS beamline, BESSY II, Germany, with a resolution of 120 meV. CrX_3 single crystals were commercially obtained from HQ Graphene, and their crystallinity was verified using laboratory-based x-ray diffraction. Due to the samples' high hygroscopicity and sensitivity to oxygen, the CrX_3 samples were stored and handled under an inert gas atmosphere (Ar) in a glovebox environment to minimize air exposure. The samples were subjected to scotch tape exfoliation before being transferred to the experimental chamber to ensure a clean surface.

B. Computational simulations

The quantum many-body script language QUANTY [29,30] was used to simulate the experimental CrX_3 XAS and RIXS spectra. The Hamiltonian that describes the electronic structure of the system was built using multiplet ligand field theory (MLFT) [29,31,32]. The relevant electronic configurations in Cr^{3+} for the RIXS process consist of a GS $2p^6 3d^3$ with an intermediate excited state $2p^5 3d^4$ followed by a de-excitation to the GS. They resulted in atomic multiplets, which are described by $3d$–$3d$ Coulomb and $2p$–$3d$ exchange interactions parametrized in Slater-Condon integrals F^k_{dd}, F^k_{pd} (Coulomb), and G^k_{pd} (exchange) for Hartree-Fock calculations [29,33]. The Racah B and Racah C parameters were used to account for the ion covalency, which can be related to the F^2_{dd} and F^4_{dd} by Racah $B = (9F^2_{dd} - 5F^4_{dd})/441$ and Racah $C = 5F^4_{dd}/63$ [34]. The ligand-to-metal charge transfer (LMCT) parameters were incorporated to account for hopping between the halide ions and Cr^{3+} metal ions.

Local symmetry is a crucial parameter that can significantly influence the electronic, magnetic, and optical properties of materials [35]. While the perfect octahedral (O_h)

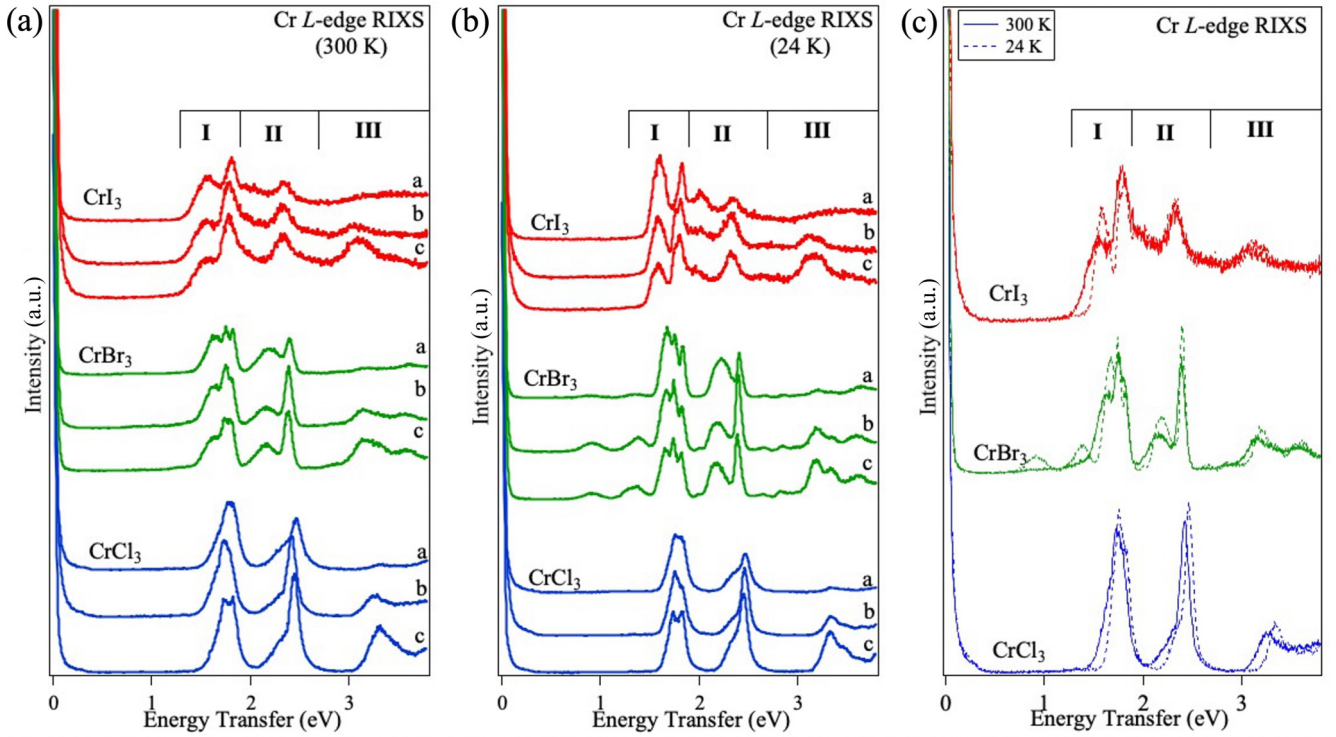

FIG. 2. Cr L_3-edge RIXS data measured in CrX_3 at (a) 300 K and (b) 24 K. The RIXS data have been collected at three different excitation energies: **a, b,** and **c** [see Fig. 1(c)]. The three regions, I, II, and III, show different spectral features in RIXS spectra. (c) Temperature comparison of the RIXS data at Cr L_3 edge. Solid (dashed) lines indicate the 300 K (24 K) RIXS data.

symmetry has been commonly assumed for the metal Cr^{3+} in CrX_3 studies [4,5,19,36,37], only a few have accounted for the actual distorted O_h orientation. The trigonal distortion in CrX_3 results in lowering the symmetry from O_h to D_{3d} and further to C_3 [9,10,18,21,26,38]. Notably, C_3 symmetry is a subgroup of the D_{3d} symmetry [39]. Since the high-resolution RIXS spectra enabled us to resolve multiple peak splittings, atomic multiplet RIXS spectra calculations using lower symmetry C_3 reproduced the experimental RIXS spectra more reliably.

III. RESULTS

A. XAS and RIXS

Figure 1(c) shows the Cr L-edge XAS spectra acquired from 570 to 600 eV at room temperature (RT) in total electron yield mode. During the XAS process, the $2p^63d^3$ GS electrons are excited to the $2p^53d^4$ state. Therefore, spectral features are dominated by dipole transitions from the core $2p$ level to the empty $3d$ states. Consequently, the two primary peaks observed in the XAS data can be attributed to the L_3 (∼575–580 eV) and L_2 (∼583–590 eV) lines [4,40]. The L_3 edge **[b** in Fig. 1(c)] in CrX_3 was determined to be 577.7, 576.8, and 576.4 eV for X = Cr, Br, and I, respectively; indicating a shift toward lower energy as the halogen changes from Cl to I.

Next, the incident photon beam was tuned to energies **a, b,** and **c**, and the RIXS measurements were performed. Figure 2(a) shows the experimental RIXS spectra measured at RT. The 0 eV feature can be attributed to the elastic feature, where the incident photon energy E_{in} equals the scattered photon energy E_{out}. The nonzero spectral features are divided into three regions: I (1.3–1.9 eV), II (1.9–2.7 eV), and III (2.7–4 eV). All three regions, I, II, and III, contain spectral features that can be attributed to the interorbital dd excitations. In this report, we only focus on d-site electronic structure and related excitations. Spectral features related to the CT process above 4 eV will be discussed elsewhere (see Fig. S1 in the Supplemental Material [41]).

In Fig. 2(a), $CrCl_3$ shows a broader single peak in region I, while $CrBr_3$ shows a shoulder feature, and CrI_3 reveals a distinct splitting between the two peaks. This splitting becomes more pronounced from Cl to I. In region II, $CrCl_3$ has a main peak with a shoulder characteristic, and $CrBr_3$ shows a clear separation between two peaks, while the shoulder characteristic in CrI_3 is dominated by the main peak in region I. Region III consists of more broadened multiple subpeaks in all three materials. The energy transfer values in the aforementioned dd regions are independent of the incident energies and are known as Raman-like losses. However, the spectral intensities change with the excitation energies (**a**–**c**). These resonant and Raman behaviors further justify the attribution of these peaks to the well-known dd excitations.

Since CrX_3 shows structural and magnetic phase transitions at different temperatures, we repeated the RIXS measurements at the low temperature (LT) of 24 K [see Figs. 2(b) and 2(c)]. At 24 K, $CrBr_3$ and CrI_3 are magnetically ordered, whereas $CrCl_3$ remains paramagnetic. The same energy regions are demarcated in the LT RIXS spectra, and the spectral features are much sharper. In particular, the intensity of the shoulder features increases at 24 K. A peak shift is also observed: In $CrBr_3$, the energy gap between the shoulder feature and main peak in region II becomes smaller at LT. Moreover,

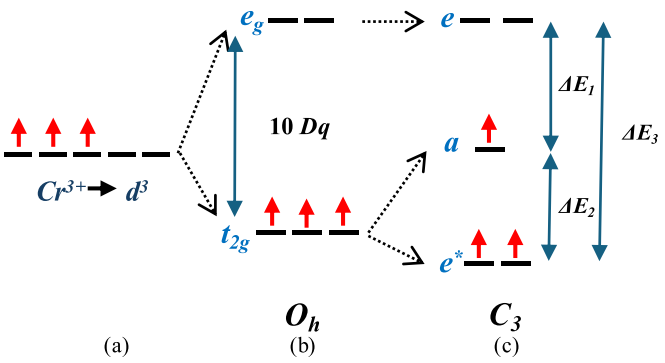

FIG. 3. (a) Valence d orbital electron distribution in Cr^{3+} metal ion. (b) Lifting of degeneracy of the d^{3+} spectroscopic term (free F^{4+} ion) due to O_h symmetry. This configuration's 5 d orbitals are divided into two energy levels t_{2g} and e_g. (c) Lifting of the degeneracy of the d^{3+} electrons due to C_3 symmetry. The five d orbitals are divided into one a state and two e states within the C_3 symmetry.

several extraneous peaks emerge in LT RIXS spectra of $CrBr_3$ between 0 and 1.5 eV. However, such features are absent in the LT RIXS data from BESSY II and Advanced Light Source [4] (see Fig. S1 in the Supplemental Material [41]). Therefore, a more extensive analysis is required to validate these LT features in the 0–1.5 eV range, and their physical origin remains unresolved.

B. Energy level diagrams and RIXS simulations

1. Energy level diagrams

In this study, electronic ELDs are utilized to analyze the spectral features observed in the experimental RIXS data. The ELDs are calculated by diagonalizing the standard ligand field multiplet Hamiltonian. The results provide the number of excited states in the system, including the spin-allowed and spin-forbidden states, which can be directly compared with the RIXS spectral features to determine the corresponding energy scales.

The multielectronic atomic states of the $Cr^{3+}(d^3)$ configuration are labeled in the diagrams. In a perfect octahedral environment with O_h symmetry, the Cr five d orbitals are split into two energy levels t_{2g} and e_g [see Fig. 3(b)]. This crystal field splitting results in the division of the 3d multielectronic atomic quartet states into manifolds: $^4F \rightarrow {}^4A_{2g}$, $^4T_{2g}$, and $^4T_{1g}(1)$, and $^4P \rightarrow {}^4T_{1g}(2)$ [4,42]. When the trigonal distortion is considered and the symmetry is lowered from O_h to C_3 (D_{3d}), the t_{2g} orbitals are further divided into two states a (a_{1g}) and e^* (e_g^*), as shown in Fig. 3(c). Within the C_3 symmetry configuration, the atomic state $^4T_{2g}$ and $^4T_{1g}$ branches into ^4A and ^4E states (see Fig. S2 in the Supplemental Material [41]) [26,33,38]. The energies of the three states e, a, and e^* can be written using the crystal field parameter Dq, and the distortion parameters $D\tau$ and $D\sigma$ as follows [29,39]:

$$E_e = 6Dq + (7/3)D\tau, \tag{1a}$$

$$E_a = -4Dq - 2D\sigma - 6D\tau, \tag{1b}$$

$$E_{e*} = -4Dq + D\sigma + (2/3)D\tau. \tag{1c}$$

The initial parameters for ELD calculations were referred from the literature corresponding to the O_h symmetry [4]. The Coulomb interaction U of 3.5 eV was used, and the ELDs do not depend on the Coulomb interaction U, and its effect on the RIXS intensity is very small [43]. The ratio between U_{dd} and U_{pd} was kept constant at 1.5 eV. Figure 4 shows the ELDs calculated as a function of the crystal field Dq, Racah B, and Racah C in CrI_3. Dashed blue and solid red lines indicate the spin-doublet and spin-quartet states, respectively. Here, we only report the ELDs for CrI_3, as it has the maximum splitting between energy states; the ELDs of $CrCl_3$ and $CrBr_3$ can be found in Figs. S3 and S4 in the Supplemental Material [41].

The crystal field splitting 10Dq can be determined by considering the electronic transition $^4A_{2g} \rightarrow {}^4T_{2g}$ states within the O_h environment [44]. This is equivalent to the first nonzero energy transfer peak maximum in experimental RIXS spectra, where the $^4T_{2g}$ state has been reported at 1.73, 1.6, and 1.45–1.58 eV for $CrCl_3$, $CrBr_3$, and CrI_3, respectively [4,9,26,45]. These values align with the shoulder feature in region I in our RIXS data. On the other hand, the sharp peaks in the optical spectroscopy can be compared directly with the dd excitations in the RIXS spectra. Optical absorption and magnetic circular dichroism measurements report the spin-allowed $^4T_{2g}$ states and bright excitons in $CrCl_3$ at 1.7–1.75 eV, $CrBr_3$ at 1.6–1.65 eV, and CrI_3 at 1.45–1.6 eV, respectively [18–21,37,46,47]. These peak positions also show good alignment with the shoulder features in region I. Therefore, considering the shoulder peak in region I and comparing that with the ELD in Fig. 4(a), the crystal field splitting 10Dq in $CrCl_3$, $CrBr_3$, and CrI_3 was determined to be 1.58, 1.54, and 1.35 eV, respectively. The corresponding electronic transition is $^4A \rightarrow {}^4E$ ($t_{2g}^3 \rightarrow t_{2g}^2 e_g^1$) for the C_3 symmetry, since the transition of orbital singlets $^4A \rightarrow {}^4A$ is dipole-forbidden. The splitting of ^4E and ^4A ($^4T_{2g}$) states can be tuned by the distortion parameter $D\sigma$, which was determined to be -20, -15, and -10 meV as the halogen changes from Cl to I (see Fig. S2 in the Supplemental Material [41]). A summary of the crystal field parameters and the energies of each state is provided in Table I.

The Racah B was varied next, and the result is presented in Fig. 4(b). The two peaks in region II were assigned to ^4A and ^4E states, and they showed an increment in the splitting as the halogen changed from Cl to I. Their expected order of states and the energy gap were dependent on the crystal field distortion parameter $D\tau$, which was determined to be 27, 33, and 35 meV for $CrCl_3$, $CrBr_3$, and CrI_3, respectively (see Fig. S2 in the Supplemental Material [41]). The electronic transition $^4A \rightarrow {}^4E$ ($^4T_{1g}$), which corresponds to the double electron excitation $t_{2g}^3 \rightarrow t_{2g}^1 e_g^2$, was considered in determining the Racah B values of 0.072, 0.071, and 0.067 eV in $CrCl_3$, $CrBr_3$, and CrI_3, respectively.

After tuning the 10Dq and Racah B values, the ELD was calculated as a function of Racah C, as shown in Fig. 4(c). At this stage, the quartet lines appear to be horizontal. However, the ELDs include several doublet states influenced by Racah B and Racah C. These doublet states represent spin-flip electronic transitions. The SOC in the Cr 2p level can accompany the spin-flip electronic transition during the RIXS process, producing spin-forbidden doublet states with $S = 1/2$, as discussed in the latter. Racah C of 0.41−0.42 eV in all CrX_3

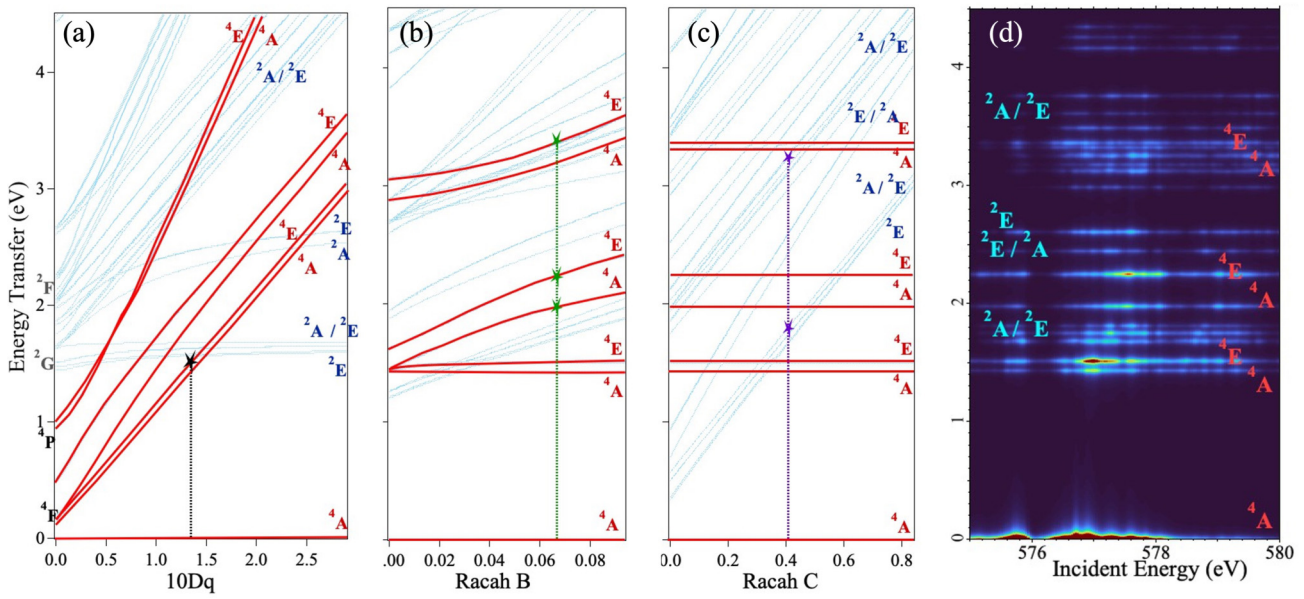

FIG. 4. Energy level diagrams as a function of (a) crystal field Dq (b) Racah B, and (c) Racah C in CrI_3. The quartet and doublet states in Cr^{3+} metal are shown by solid red and dashed blue lines, respectively. The black, green, and purple stars indicate the extracted Dq, Racah B, and Racah C values by comparing the ELDs with experimental RIXS spectra. (d) Calculated RIXS map recorded at 300 K. A broadening of 30 meV was considered, similar to the experimental resolution.

was determined after considering the transitions $^4A \rightarrow {}^2A$ and $^4A \rightarrow {}^2E$ ($^2T_{1g}$). A summary of the energy scales calculated in CrX_3 at RT is provided in Table II.

2. XAS/RIXS spectrum calculation

The XAS experimental data were used to tune the RIXS intermediate parameters, as the RIXS process consists of an XAS process followed by a resonant x-ray emission (see Fig. S5 in the Supplemental Material [41]). The Slater integral parameters F^2_{pd}, G^1_{pd}, and G^3_{pd}, which account for the electron exchange interactions $2p3d$, were tuned to match the experimental XAS data. Furthermore, the $2p_{3/2}$ and $2p_{1/2}$ spectral parts are clearly separated by the core-hole SOC and the core-hole lifetime broadening, which gives the sharp features [48]. The energy separation of 8.5 eV between the L_3 and L_2 peaks [Fig. 1(c)] suggested a Cr $2p$ SOC value of ~5.7 eV.

Subsequently, we calculated the RIXS spectra using all refined parameters and compared the results with the experimental RIXS data, as illustrated in Fig. 5. In each figure, the top panel shows the experimental RIXS data measured at the Cr L_3 edge. The middle panel shows the calculated RIXS spectra analogs of the top panel. The RIXS spectra calculated with a broadening of 30 meV (red shaded line) exhibit fine spectral features and energy positions that are responsible for the main intensities in the experimental data. We only reported the results at the L_3 edge (excitation energy **b**) in Fig. 5. Similar results were obtained for all the excitation energies [see the RIXS map in Fig. 4(c)]. The peak positions extracted from the simulated RIXS spectra are shown in the bottom panel with red lines indicating spin-allowed quartet states and blue lines indicating spin-flip doublet states. Figure 5 clearly demonstrates the RIXS ability to probe states with different spin multiplicities selectively.

A clear energy gap between the spin-allowed quartets and spin-forbidden doublets in regions I and II was observed with high resolution in RIXS data. This energy difference becomes more prominent as the halogen changes from Cl to Br to I, which explains the appearance of a shoulder feature as the halogen changes from Cl to I in the experimental RIXS data (see Fig. 5). Two peaks observed in region II primarily depend on the crystal field distortion parameter $D\tau$ as they can be attributed to ^4A and ^4E states and result in improved RIXS fitting using the distorted octahedral orientation with C_3 symmetry in CrX_3. There is a slight mismatch between the experimental RIXS data and the simulated RIXS spectra

TABLE I. Summary of the crystal field splitting parameters and the energy levels in Cr d orbitals in CrX_3.

	T	$10Dq$	$D\tau$	$D\sigma$	E_e	E_a	E_{e*}	ΔE_1	ΔE_2	ΔE_3
$CrCl_3$	300 K	1.580	0.027	−0.020	1.011	−0.754	−0.634	1.765	−0.120	1.645
$CrBr_3$	300 K	1.540	0.033	−0.015	1.001	−0.784	−0.609	1.785	−0.175	1.610
CrI_3	300 K	1.350	0.035	−0.010	0.892	−0.730	−0.527	1.622	−0.203	1.418
$CrCl_3$	24 K	1.620	0.020	−0.020	1.019	−0.728	−0.655	1.747	−0.073	1.673
$CrBr_3$	24 K	1.540	0.028	−0.015	0.989	−0.754	−0.612	1.743	−0.142	1.602
CrI_3	24 K	1.370	0.035	−0.010	0.904	−0.738	−0.535	1.642	−0.203	1.438

TABLE II. Summary of the electronic structure parameters calculated at 300 K for CrX_3. All values are in eV.

	$CrCl_3$ ($3d^3$)	$CrCl_3$ ($2p^5 3d^4$)	$CrBr_3$ ($3d^3$)	$CrBr_3$ ($2p^5 3d^4$)	CrI_3 ($3d^3$)	CrI_3 ($2p^5 3d^4$)
Racah B	0.072	0.077	0.071	0.076	0.067	0.072
Racah C	0.410	0.441	0.420	0.452	0.410	0.441
F^2_{dd}	6.398 (59%)	6.884 (59%)	6.419 (60%)	6.907 (60%)	6.153 (57%)	6.620 (57%)
F^4_{dd}	5.166 (76%)	5.561 (76%)	5.292 (78%)	5.696 (78%)	5.166 (76%)	5.561 (76%)
F^2_{pd}	–	5.873 (90%)	–	5.546 (85%)	–	5.220 (90%)
G^1_{pd}	–	3.254 (68%)	–	3.110 (65%)	–	2.871 (60%)
G^3_{pd}	–	1.633 (60%)	–	1.361 (50%)	–	1.088 (40%)
SOC_{3d}	0.018 (50%)	0.018 (50%)	0.018 (50%)	0.018 (50%)	0.018 (50%)	0.018 (50%)
SOC_{2p}	–	5.668 (100%)	–	5.668 (100%)	–	5.668 (100%)
J_H	0.826	0.889	0.837	0.900	0.809	0.870
Δ	3.800	3.800	3.300	3.300	3.000	3.000
$10DqL$	0.103	0.103	0.238	0.238	0.032	0.032
V_e	1.992	1.992	1.940	1.940	1.836	1.836
V_{a1}	1.320	1.320	1.380	1.380	1.400	1.400
V^*_e	1.320	1.320	1.380	1.380	1.400	1.400

in region III due to the cluster of doublets (see Fig. 4) and CT excitations, which we have not discussed in this study. As the temperature is lowered to 24 K, the shift in the RIXS spectral features in region I [see Fig. 2(c)] results in higher $10Dq$ values and thus a greater crystal field splitting at LT. This increase in splitting will enhance the single-ion magnetic anisotropy, which helps stabilize the magnetic order at LT, requiring more energy to probe the $t_{2g} \rightarrow e_g$ excitation

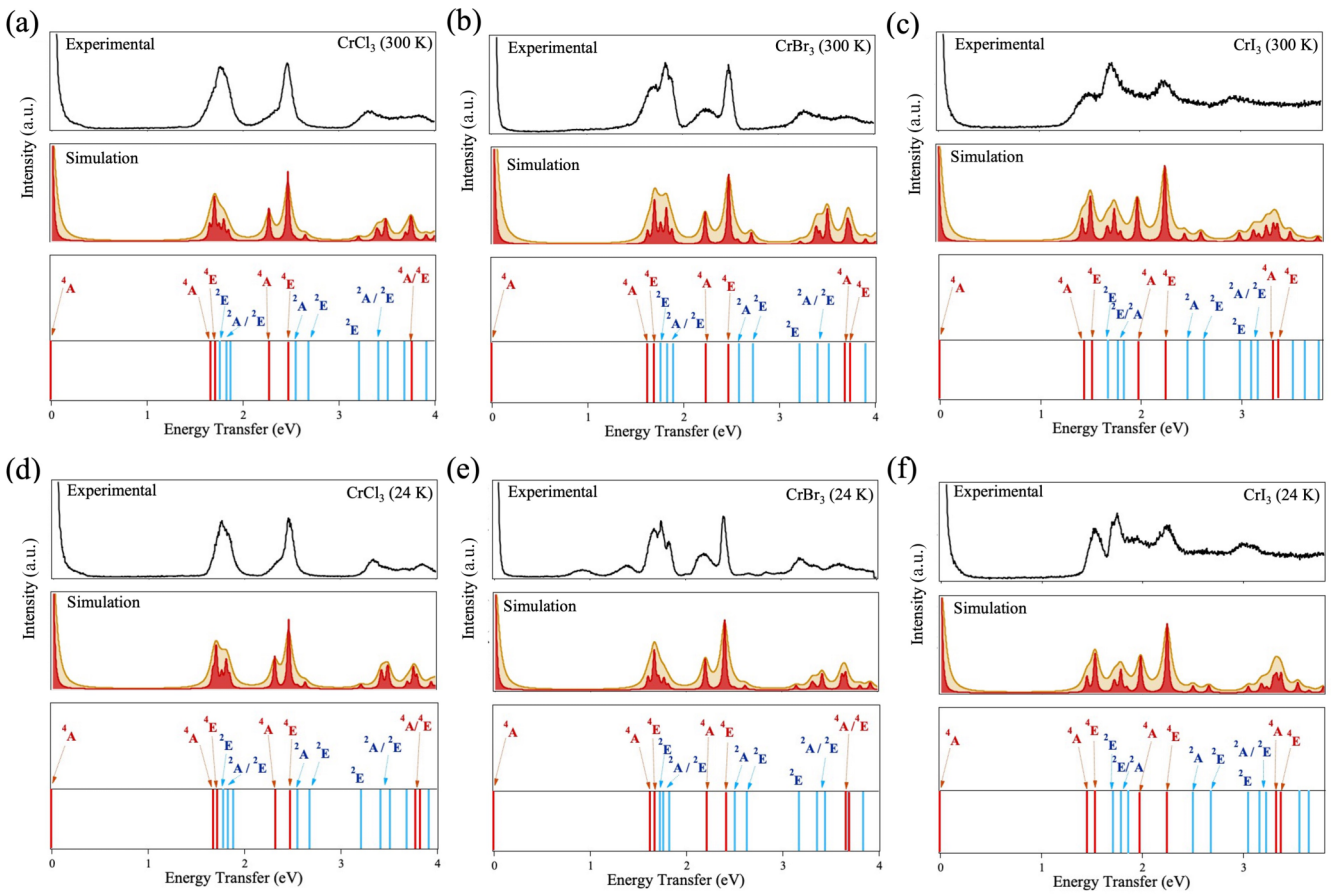

FIG. 5. Comparison of experimental and simulated RIXS spectra at Cr L_3 edge (a)–(c) at 300 K and (d)–(f) at 24 K in $CrCl_3$, $CrBr_3$, and CrI_3, respectively. In each figure, the top panel and the middle panels show the experimental and simulated RIXS spectra at the Cr L_3 edge. Bottom panel indicates the spectroscopic term labels given in C_3 symmetry, analogous to the middle panel.

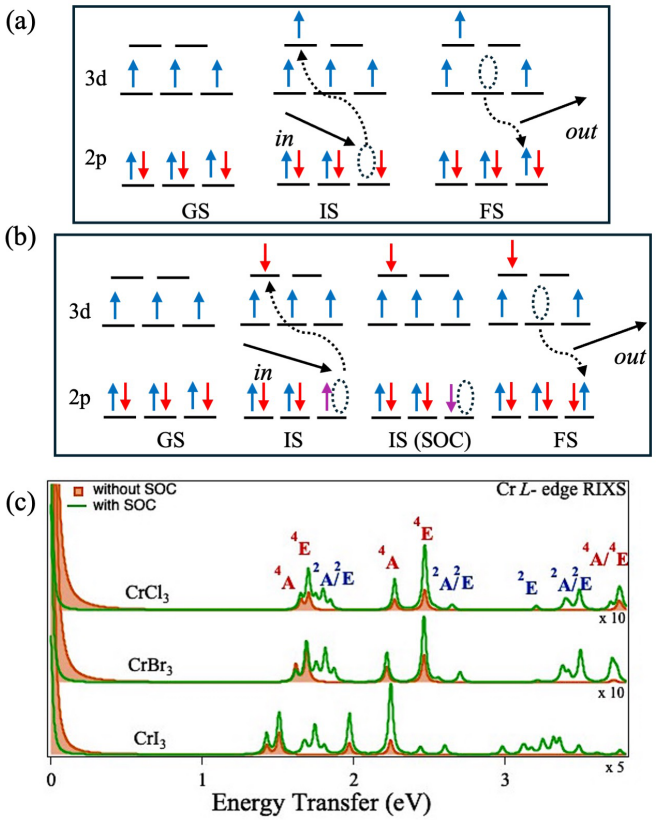

FIG. 6. (a) Electronic excitation corresponds to the spin-allowed quartet state. The GS, IS, and FS electron configurations are indicated. The spin moment is conserved throughout the process. (b) Electronic excitation for the spin-flip doublet state. The incident and scattered x-rays are labeled as in and out, respectively. (c) Comparison of RIXS spectra with the contribution of SOC (green) and without SOC (brown) in the Cr metal ion.

[49,50]. In region II, the shift in CrI_3 is negligible. The peak shift in $CrCl_3$ and $CrBr_3$ can be explained by $D\tau$ and Racah B. Since CrX_3 exhibits both MPT and SPT at different temperatures, the SPT can possibly cause a change in octahedral distortion, resulting in different crystal field distortion parameters and, consequently, different electronic structure parameters.

A schematic representation of Cr $2p3d$ RIXS in Figs. 6(a) and 6(b) shows the electronic excitations from the initial GS through the intermediate core-excited to the final valence-excited states. Figure 6(a) captures the electronic excitation corresponding to the spin-allowed quartet states, where the total spin moment of the GS and the final state (FS) is $S = 3/2$ ($2S + 1 = 4$), indicating a conserved spin moment during the RIXS process. On the other hand, Fig. 6(b) shows the electronic excitation that corresponds to the spin-forbidden (spin-flip) doublet states, where the total spin moment changes from $S = 3/2$ to $S = 1/2$ ($2S + 1 = 2$) from the GS to the final state, indicating a spin-flip during the process. The presence of Cr $2p$ SOC [given by the Cr $2p$ spin-orbit parameter $\zeta(2p)$ (5.668 eV)], which is much stronger than the $3d$ SOC [given by the Cr $3d$ spin-orbit parameter $\zeta(3d)$ (0.018 eV)], contributes to this spin-flip process and enables the probing of spin-forbidden states [19,48]. Figure 6(c) compares the RIXS spectra calculated with the SOC (green line) and without SOC (brown curve). Spectra without SOC do not produce the spin-forbidden doublet states, disagreeing with the experimental data. Therefore, our calculation suggests that SOC must be considered in RIXS calculations in order to probe the spin-forbidden doublet states.

IV. DISCUSSION

Based on high-resolution RIXS spectra for CrX_3, a detailed electronic structure parameter calculation was presented, including the determination of the crystal field splitting and Racah parameters in CrX_3. Now, we discuss how the obtained values relate to previously determined electronic structure parameters in CrX_3. The extracted energies of the spin-quartet and spin-doublet states are consistent with the d^3 ELDs in Cr^{3+} systems [4,33]. Density functional theory calculations predict that the magnetic moment is hosted predominantly in the Cr^{3+} ions with $S = 3/2$ spin configuration and a reported spin moment of $3\,\mu_B$/Cr [3,51,52]. From our calculations, the spin moment of the Cr was determined to be $\sim$3.75 μ_B/Cr, indicating a larger value compared to the nominal spin moment in Cr due to the ligand contribution [4,53].

The reported $10Dq$ values in $CrCl_3$ (1.50–1.75 eV), $CrBr_3$ (1.45–1.65 eV), and CrI_3 (1.30–1.45 eV) exhibit significant overlap and variability, indicating inconsistency and a variance in the determined values [4,9,18,19,21,26]. This makes it hard to draw firm conclusions about the trend in the ligand field strength. The improved energy resolution from our RIXS measurements enabled further refinement of the $10Dq$ parameter using C_3 symmetry with distorted octahedral orientation across all halides. As the halogen changes from Cl to Br to I, a clearly decreasing trend is observed in the refined $10Dq$ values from our study (1.58, 1.54, and 1.35 eV for $CrCl_3$, $CrBr_3$, and CrI_3, respectively). This is in good agreement with the spectrochemical series explaining the strength of various ligand-induced crystal fields: $I^{-1} < Br^{-1} < Cl^{-1}$ [54]. This work highlights the need for high-resolution RIXS measurements when it comes to determining precise electronic structure parameters.

The determined crystal field distortion parameters (see Table I) show an opposite sign relation: negative for $D\sigma$ and positive for $D\tau$. As the halogen changes from Cl to I, the $D\sigma$ and $D\tau$ show incremental changes, suggesting a higher (lower) distortion in CrI_3 ($CrCl_3$). A similar study reports the distortion parameters for CrI_3: $D\sigma = -0.3$ eV and $D\tau = 0$ eV, and CrF_2: $Ds = -0.2$ eV and $Dt = 0.2$ eV, showing a good agreement with our results [9,55]. The determined crystal field parameters were applied to Eqs. (1a)–(1c) to calculate the energies of the states e, a, and e^* as summarized in Table I and graphically represented in Fig. 7. The results suggest that a state has the lowest energy. A similar 2D van der Waals family VX_3 reports a trigonal contraction when the a state is lowest, and our results suggest a similar behavior in CrX_3 [56,57]. The energy gap between each state is given by ΔE_1, ΔE_2, and ΔE_3 (see Fig. 3) as summarized in Table I. The energy gap between the highest and lowest states (ΔE_3)

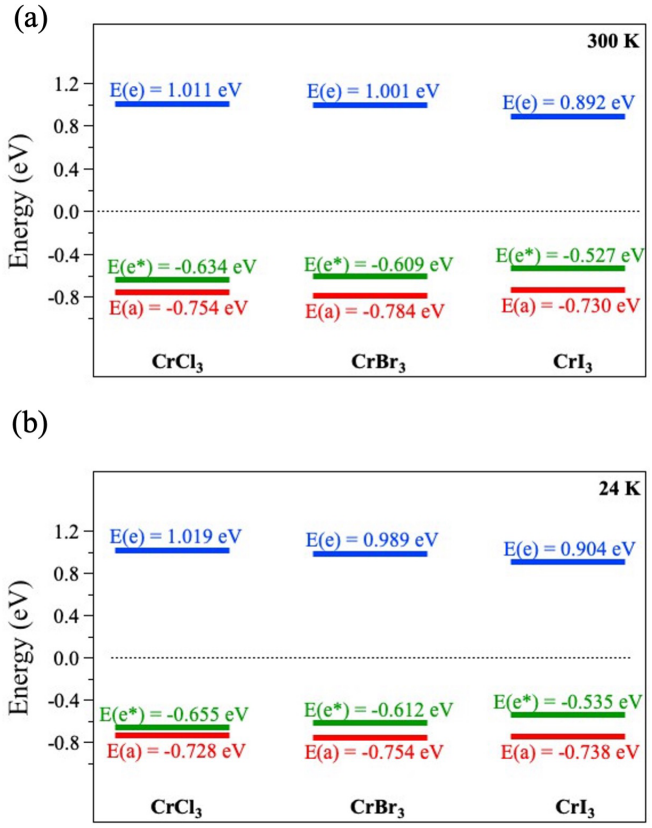

FIG. 7. The calculated energy levels of the Cr d orbitals in $CrCl_3$, $CrBr_3$, and CrI_3 at (a) 300 K and (b) 24 K.

decreases as the halogen changes from Cl to I, consistent with the $10Dq$ trend.

A summary of the electronic structure parameters used in the RIXS simulations at 300 K is provided in Table II, including the LMCT parameters (see Table S1 in the Supplemental Material [41] for the electronic structure parameters at 24 K). Note that the unequal scaling in Hartree-Fock Slater integrals F^2_{dd} and F^4_{dd} and the exchange parameters G^1_{pd} and G^3_{pd} are essential to reproduce the RIXS spectra. The Racah B parameter, which accounts for interelectronic repulsion, shows a decreasing trend as the halogen changes from Cl to Br to I, agreeing with the nephelauxetic effect. These values reflect the increasing covalency that is observed from Cl < Br < I with higher scaling of the Hartree-Fock parameters corresponding to the ionic interactions and lower scaling corresponding to the covalent interactions [4,10,31,54]. The determined Racah B values show a good agreement with the reported values, which are in range of 0.067–0.095, 0.062–0.09, and 0.047–0.087 for $CrCl_3$, $CrBr_3$, and CrI_3, respectively [4,10]. The Racah C values do not change as the halogen varies. The Racah A ($A = F^0_{dd} - F^4_{dd}/9$) was ignored because it is considered the same for any metal ion. The determined C/B ratios at RT of 5.69, 5.92, and 6.12 were lower than the literature-reported values and closer to the expected value of 3.75–4. The Racah B parameter primarily determines the ratio C/B, as the Racah C is constant. It increases with the halogen change from Cl to I, reflecting the shift from ionic bonding in $CrCl_3$ to covalent bonding in CrI_3. The Hund's exchange coupling $J_H = (F^2_{dd} + F^4_{dd})/14$ for $CrCl_3$, $CrBr_3$, and CrI_3 was calculated to be 0.826, 0.837, and 0.809 eV, respectively [4,5]. These values indicate that all CrX_3 materials are in the high-spin state, given the relation $2J_H < 10Dq$ [58].

The SOC in CrX_3 plays a significant role in the spin-flip (spin-forbidden) process, as discussed earlier. Recent studies suggest that the spin-flip excitations are responsible for the anisotropic SOC, which, in turn, contributes to the Dzyaloshinskii-Moriya (DM) interaction [9,59]. However, further investigations are needed to better understand the relationship between the strength of SOC and its influence on the DM interaction. This study lays an important foundation for future investigations into CrX_3 as a material for spintronic and optoelectronic devices, where precise control over electronic and optical properties is crucial for achieving advanced functionalities.

V. CONCLUSIONS

We conducted Cr $2p-3d$ XAS and Cr L-edge high-resolution RIXS measurements on CrX_3. Atomic multiplet RIXS simulations, interpreted using the MLFT approach, showed good agreement with the experimental RIXS data, as illustrated in Fig. 5. This study marks the first experimental observation of clear energy separations between spin-allowed and spin-forbidden electronic transitions in CrX_3 using the improved high-resolution RIXS measurements. By applying ELDs in atomic multiplet calculations, we have refined the electronic energy scales, taking into account the distorted octahedral orientation with C_3 symmetry in CrX_3, as detailed in Tables I and II. These findings indicate that the ligand substitution significantly affects the d-orbital electronic structure. The superexchange coupling effect on the interatomic orbital splitting was discussed, as well as the DM interactions and the role of SOC in the spin-forbidden excitations. We propose that investigating RIXS on few-layer CrX_3 samples could offer deep insights into the electronic structure properties of these materials. Further investigations are needed to understand the low-energy RIXS spectral features in the 0–1.5 eV range.

ACKNOWLEDGMENTS

This research was conducted at 41A RIXS beamline, Taiwan Photon Source (TPS), and PEAXIS RIXS beamline, BESSY II, Germany operated by the Helmholtz-Zentrum Berlin für Materialien und Energie. The preliminary RIXS measurements were taken at the qRIXS 8.0.1 beamline, Advanced Light Source (ALS), which is a DOE Office of Science User Facility under Contract no. DE-AC02-05CH11231. We thank all the beamline scientists for their valuable support. Y.C.S. acknowledges the financial support from the National Science and Technology Council (NSTC) in Taiwan under Grant No. 113-2112-M-213-025-MY3. The Welch Foundation (Grant No. E-0001) and the Texas Center for Superconductivity (TCSUH) supported work at the University of Houston. Part of this work was supported by the U.S. DOE, BES, under Award No. DE-SC0024332. The authors acknowledge support from the U.S. Air Force Office of Scientific Research and Clark-

son Aerospace Corp. under Award No. FA9550-21-1-0460. Special thanks to the eXn group members at the University of Houston.

DATA AVAILABILITY

The data that support the findings of this study are available from the corresponding author upon reasonable request.

[1] S. Mondal, A. Midya, M. M. Patidar, V. Ganesan, and P. Mandal, Magnetic and magnetocaloric properties of layered van der Waals $CrCl_3$, Appl. Phys. Lett. **117**, 092405 (2020).

[2] I. Tsubokawa, On the magnetic properties of a $CrBr_3$ single crystal, J. Phys. Soc. Jpn. **15**, 1664 (1960).

[3] M. A. McGuire, H. Dixit, V. R. Cooper, and B. C. Sales, Coupling of crystal structure and magnetism in the layered, ferromagnetic insulator CrI_3, Chem. Mater. **27**, 612 (2015).

[4] Y. C. Shao, B. Karki, W. Huang, X. Feng, G. Sumanasekera, J.-H. Guo, Y.-D. Chuang, and B. Freelon, Spectroscopic determination of key energy scales for the base Hamiltonian of chromium trihalides, J. Phys. Chem. Lett. **12**, 724 (2021).

[5] L. Craco, S. S. Carara, Y.-C. Shao, Y.-D. Chuang, and B. Freelon, Electronic structure of rhombohedral CrX_3 (X = br, cl, I) van der Waals crystals, Phys. Rev. B **103**, 235119 (2021).

[6] J. C. A. Boeyens, The periodic electronegativity table, Z. Naturforsch. B **63**, 199 (2008).

[7] J. B. Goodenough, *Magnetism and the Chemical Bond* (Robert E. Kreiger Publishing Company Huntingdon, New York, 1976).

[8] N. D. Mermin and H. Wagner, Absence of ferromagnetism or antiferromagnetism in one- or two-dimensional isotropic Heisenberg models, Phys. Rev. Lett. **17**, 1133 (1966).

[9] A. Ghosh, H. J. M. Jönsson, D. J. Mukkattukavil, Y. Kvashnin, D. Phuyal, P. Thunström, M. Agåker, A. Nicolaou, M. Jonak, R. Klingeler *et al.*, Magnetic circular dichroism in the dd excitation in the van der Waals magnet CrI_3 probed by resonant inelastic x-ray scattering, Phys. Rev. B **107**, 115148 (2023).

[10] M. Atanasov, D. Ganyushin, K. Sivalingam, and F. Neese, A modern first-principles view on ligand field theory through the eyes of correlated multireference wavefunctions, in *Molecular Electronic Structures of Transition Metal Complexes II*, edited by D. M. P. Mingos, P. Day, and J. P. Dahl (Springer, Heidelberg, Dordrecht, London, New York, 2012), pp. 149–220.

[11] S. Jiang, L. Li, Z. Wang, K. F. Mak, and J. Shan, Controlling magnetism in 2D CrI_3 by electrostatic doping, Nat. Nanotechnol. **13**, 549 (2018).

[12] K. S. Novoselov, A. Mishchenko, A. Carvalho, and A. H. Castro Neto, 2D materials and van der Waals heterostructures, Science **353**, aac9439 (2016).

[13] L. Pan, L. Huang, M. Zhong, X.-W. Jiang, H.-X. Deng, J. Li, J.-B. Xia, and Z. Wei, Large tunneling magnetoresistance in magnetic tunneling junctions based on two-dimensional CrX_3 (X = Br, I) monolayers, Nanoscale **10**, 22196 (2018).

[14] M. Akram, H. LaBollita, D. Dey, J. Kapeghian, O. Erten, and A. S. Botana, Moiré skyrmions and chiral magnetic phases in twisted CrX_3 (X = I, Br, and Cl) bilayers, Nano Lett. **21**, 6633 (2021).

[15] S. R. Singamaneni, L. M. Martinez, J. Niklas, O. G. Poluektov, R. Yadav, M. Pizzochero, O. V. Yazyev, and M. A. McGuire, Light induced electron spin resonance properties of van der Waals CrX_3 (X = Cl, I) crystals, Appl. Phys. Lett. **117**, 082406 (2020).

[16] P. Mishra and T. Baruah, Magnetic properties of CrX_3 (X = Cl, Br, I) monolayers in excited states, J. Mater. Chem. C **12**, 5213 (2024).

[17] A. S. Ahmad, Y. Liang, M. Dong, X. Zhou, L. Fang, Y. Xia, J. Dai, X. Yan, X. Yu, J. Dai *et al.*, Pressure-driven switching of magnetism in layered $CrCl_3$, Nanoscale **12**, 22935 (2020).

[18] I. Pollini and G. Spinolo, Intrinsic optical properties of $CrCl_3$, Phys. Status Solidi B **41**, 691 (1970).

[19] J. F. Dillon, Jr., H. Kamimura, and J. P. Remeika, Magneto-optical studies of chromium tribromide, J. Appl. Phys. **34**, 1240 (1963).

[20] C. Limido, G. Pedroli, and G. Spinolo, Specific magnetic rotation in the crystal field bands of $CrCl_3$, Solid State Commun. **11**, 1385 (1972).

[21] V. M. Bermudez and D. S. McClure, Spectroscopic studies of the two-dimensional magnetic insulators chromium trichloride and chromium tribromide—I, J. Phys. Chem. Solids **40**, 129 (1979).

[22] S. Sugano, *Multiplets of Transition-Metal Ions in Crystals* (Academic Press, New York, London, 1970).

[23] M. I. Katsnelson and A. I. Lichtenstein, Theory of optically forbidden $d-d$ transitions in strongly correlated crystals, J. Phys.: Condens. Matter **22**, 382201 (2010).

[24] A. Singh, H. Y. Huang, Y. Y. Chu, C. Y. Hua, S. W. Lin, H. S. Fung, H. W. Shiu, J. Chang, J. H. Li, J. Okamoto *et al.*, Development of the soft x-ray AGM-AGS RIXS beamline at the Taiwan Photon Source, J. Synchrotron Radiat. **28**, 977 (2021).

[25] L. J. P. Ament, M. Van Veenendaal, T. P. Devereaux, J. P. Hill, and J. Van Den Brink, Resonant inelastic x-ray scattering studies of elementary excitations, Rev. Mod. Phys. **83**, 705 (2011).

[26] C. A. Occhialini, L. Nessi, L. G. P. Martins, A. K. Demir, Q. Song, V. Hasse, C. Shekhar, C. Felser, K. Watanabe, T. Taniguchi *et al.*, Spin-forbidden excitations in the magneto-optical spectra of CrI_3 tuned by covalency, Phys. Rev. X **15**, 031005 (2025).

[27] M. L. Baker, M. W. Mara, J. J. Yan, K. O. Hodgson, B. Hedman, and E. I. Solomon, K- and L-edge x-ray absorption spectroscopy (XAS) and resonant inelastic x-ray scattering (RIXS) determination of differential orbital covalency (DOC) of transition metal sites, Coord. Chem. Rev. **345**, 182 (2017).

[28] R.-P. Wang, B. Liu, R. J. Green, M. U. Delgado-Jaime, M. Ghiasi, T. Schmitt, M. M. van Schooneveld, and F. M. F. De Groot, Charge-transfer analysis of $2p3d$ resonant inelastic x-ray scattering of cobalt sulfide and halides, J. Phys. Chem. C **121**, 24919 (2017).

[29] M. W. Haverkort, Quanty for core level spectroscopy—excitons, resonances and band excitations in time and frequency domain, J. Phys.: Conf. Ser. **712**, 012001 (2016).

[30] M. Retegan and S. Kuschel, Mretegan/crispy: v0.7.4, 2023, doi:10.5281/zenodo.1008184.

[31] M. W. Haverkort, M. Zwierzycki, and O. K. Andersen, Multiplet ligand-field theory using Wannier orbitals, Phys. Rev. B **85**, 165113 (2012).

[32] F. De Groot and A. Kotani, *Core Level Spectroscopy of Solids* (CRC Press, Taylor & Francis Group, New York, 2008).

[33] M. O. J. Y. Hunault, Y. Harada, J. Miyawaki, J. Wang, A. Meijerink, F. M. F. De Groot, and M. M. Van Schooneveld, Direct observation of $Cr^{3+}3d$ states in ruby: Toward experimental mechanistic evidence of metal chemistry, J. Phys. Chem. A **122**, 4399 (2018).

[34] G. Racah, Theory of complex spectra. I, Phys. Rev. **61**, 186 (1942).

[35] M. O. J. Y. Hunault, L. Galoisy, G. Lelong, M. Newville, and G. Calas, Effect of cation field strength on Co^{2+} speciation in alkali-borate glasses, J. Non-Cryst. Solids **451**, 101 (2016).

[36] K. L. Seyler, D. Zhong, D. R. Klein, S. Gao, X. Zhang, B. Huang, E. Navarro-Moratalla, L. Yang, D. H. Cobden, M. A. McGuire *et al.*, Ligand-field helical luminescence in a 2D ferromagnetic insulator, Nat. Phys. **14**, 277 (2018).

[37] W. He, J. Sears, F. Barantani, T. Kim, J. W. Villanova, T. Berlijn, M. Lajer, M. A. McGuire, J. Pelliciari, V. Bisogni *et al.*, Dispersive dark excitons in van der Waals ferromagnet CrI_3, Phys. Rev. X **15**, 011042 (2025).

[38] J. F. Dillon, H. Kamimura, and J. P. Remeika, Magneto-optical properties of ferromagnetic chromium trihalides, J. Phys. Chem. Solids **27**, 1531 (1966).

[39] A. Juhin, C. Brouder, M.-A. Arrio, D. Cabaret, P. Sainctavit, E. Balan, A. Bordage, A. P. Seitsonen, G. Calas, S. G. Eeckhout *et al.*, X-ray linear dichroism in cubic compounds: The case of Cr^{3+} in $MgAl_2O_4$, Phys. Rev. B **78**, 195103 (2008).

[40] M. Serri, G. Cucinotta, L. Poggini, G. Serrano, P. Sainctavit, J. Strychalska-Nowak, A. Politano, F. Bonaccorso, A. Caneschi, R. J. Cava *et al.*, Enhancement of the magnetic coupling in exfoliated $CrCl_3$ crystals observed by low-temperature magnetic force microscopy and x-ray magnetic circular dichroism, Adv. Mater. **32**, 2000566 (2020).

[41] See Supplemental Material at http://link.aps.org/supplemental/10.1103/jdxn-5lw4 for additional RIXS data, determination of the crystal field distortion parameters, ELDs and RIXS simulation results in $CrCl_3$ and $CrBr_3$, XAS simulation results in CrX_3, and electronic structure parameters at 24 K.

[42] V. Vercamer, M. O. J. Y. Hunault, G. Lelong, M. W. Haverkort, G. Calas, Y. Arai, H. Hijiya, L. Paulatto, C. Brouder, M.-A. Arrio *et al.*, Calculation of optical and K pre-edge absorption spectra for ferrous iron of distorted sites in oxide crystals, Phys. Rev. B **94**, 245115 (2016).

[43] S. Feldkemper and W. Weber, Generalized calculation of magnetic coupling constants for Mott-Hubbard insulators: Application to ferromagnetic Cr compounds, Phys. Rev. B **57**, 7755 (1998).

[44] M . Dalal, *A Textbook of Inorganic Chemistry* (Dalal Institute, India, 2017), Vol. 1.

[45] H. L. Schläfer and G. Gliemann, *Basic Principles of Ligand Field Theory* (Wiley-Interscience, New York, 1969).

[46] I. Pollini, J. Thomas, B. Carricaburu, and R. Mamy, Optical and electron energy loss experiments in ionic $CrBr_3$ crystals, J. Phys.: Condens. Matter **1**, 7695 (1989).

[47] S. Acharya, D. Pashov, A. N. Rudenko, M. Rösner, M. van Schilfgaarde, and M. I. Katsnelson, Real-and momentum-space description of the excitons in bulk and monolayer chromium tri-halides, npj 2D Materials Appl. **6**, 33 (2022).

[48] G. Van der Laan and I. W. Kirkman, The $2p$ absorption spectra of $3d$ transition metal compounds in tetrahedral and octahedral symmetry, J. Phys.: Condens. Matter **4**, 4189 (1992).

[49] W.-C. Zheng, G.-M. Jia, L. He, and W.-Q. Yang, A theoretical study on the temperature dependence of zero-field splitting for the tetragonal Cr^{3+} center in MgO crystal, Spectrochim. Acta, Part A **78**, 818 (2011).

[50] Y. O. Kvashnin, A. Bergman, A. I. Lichtenstein, and M. I. Katsnelson, Relativistic exchange interactions in CrX_3 (X = Cl, Br, I) monolayers, Phys. Rev. B **102**, 115162 (2020).

[51] A. Molina-Sánchez, G. Catarina, D. Sangalli, and J. Fernandez-Rossier, Magneto-optical response of chromium trihalide monolayers: Chemical trends, J. Mater. Chem. C **8**, 8856 (2020).

[52] J. F. Dillon, Jr. and C. E. Olson, Magnetization, resonance, and optical properties of the ferromagnet CrI_3, J. Appl. Phys. **36**, 1259 (1965).

[53] X. Liu, D. Legut, and Q. Zhang, Light-induced ultrafast enhancement of magnetic orders in monolayer CrX_3, J. Phys. Chem. C **127**, 13398 (2023).

[54] A. L. Tchougréeff and R. Dronskowski, Nephelauxetic effect revisited, Int. J. Quantum Chem. **109**, 2606 (2009).

[55] J. Jiménez-Mier, P. Olalde-Velasco, W.-L. Yang, and J. Denlinger, X-ray absorption and resonant inelastic x-ray scattering (RIXS) show the presence of Cr at the surface and in the bulk of CrF_2, AIP Conf. Proc. **1671**, 020002 (2015).

[56] R. Sant, A. De Vita, V. Polewczyk, G. M. Pierantozzi, F. Mazzola, G. Vinai, G. van der Laan, G. Panaccione, and N. B. Brookes, Anisotropic hybridization probed by polarization dependent x-ray absorption spectroscopy in VI_3 van der Waals Mott ferromagnet, J. Phys.: Condens. Matter **35**, 405601 (2023).

[57] L. Camerano and G. Profeta, Symmetry breaking in vanadium trihalides, 2D Mater. **11**, 025027 (2024).

[58] K. Tomiyasu, J. Okamoto, H.-Y. Huang, Z.-Y. Chen, E. P. Sinaga, W.-B. Wu, Y.-Y. Chu, A. Singh, R.-P. Wang, F. M. F. De Groot *et al.*, Coulomb correlations intertwined with spin and orbital excitations in $LaCoO_3$, Phys. Rev. Lett. **119**, 196402 (2017).

[59] J. Miyawaki, S. Suga, H. Fujiwara, M. Urasaki, H. Ikeno, H. Niwa, H. Kiuchi, and Y. Harada, Dzyaloshinskii-Moriya interaction in α-Fe_2O_3 measured by magnetic circular dichroism in resonant inelastic soft x-ray scattering, Phys. Rev. B **96**, 214420 (2017).